Computers & Fluids 51 (2011) 145–156

Contents lists available at SciVerse ScienceDirect

Computers & Fluids

journal homepage: www.elsevier.com/locate/compfluid

# Two dimensional shallow-water flow model with immersed boundary method

Hau-Rong Chung [a], Te-Yung Hsieh [b,*], Jinn-Chuang Yang [a,c]

[a] Department of Civil Engineering, National Chiao Tung University, Taiwan, ROC
[b] Environmental Informatics and Geohazards Investigation Department, Green Energy and Environment Research Laboratories, Industrial Technology Research Institute, Rm. 106, Bldg. 24, 195 Sec. 4, Chun Hsing Rd., Chutung, Hsinchu 31040, Taiwan, ROC
[c] Department of Civil Engineering, Disaster Prevention and Water Environment Research Center, National Chiao Tung University, Taiwan, ROC

ARTICLE INFO

*Article history:*
Received 28 October 2010
Received in revised form 21 April 2011
Accepted 10 August 2011
Available online 24 August 2011

*Keywords:*
Immersed boundary method
Shallow-water flow
Depth averaged
Two-dimensional flow model

ABSTRACT

This study demonstrates an immersed boundary (IB) method which integrates a depth-averaged two dimensional flow model is proposed to tackle a typical fluid–solid phase problem in fluid dynamics field. The finite-difference scheme with curvilinear coordinate system is employed to discretize the shallow-water flow equations. Lagrangian markers and Eulerian grid are applied to portray the geometric contour of interior boundary and discretize the flow domain, respectively. The Dirac delta function is accordingly conducted to link both Lagrangian and Eulerian coordinate systems. The numerical simulations of single pier are performed and compared to examine the effect of marker's mesh width, grid size, and the various Dirac delta functions. Experimental data from literatures are compared with numerical results to justify the validity of the proposed IB model. To further demonstrate the model capability, the model is applied to the hypothetical cases of piers in parallel, and compared with theoretical results.

© 2011 Elsevier Ltd. All rights reserved.

## 1. Introduction

In open channel flow, arbitrary non-submerged obstacles, such as bridges and spur dike, are typical fluid–solid phase problems in computational fluid dynamics. As far as numerical scheme concerned, commonly used methods for solving these problems include finite-element method (Taylor and Hughes [1], Molinas and Hafez [2]), finite-volume method based on triangular grid (Mingham and Causon [3]; Biglari and Sturm [4]) and finite-difference model (Tingsanchali and Maheswaran [5]). The most convenient capability of finite-element and finite-volume methods is that the triangular grid can perfectly describe the arbitrary interior boundary. However, as far as grid generation concerned, the advantages for finite-difference model with quadrangular grid are simple and convenient. Tingsanchali and Maheswaran [5] developed a finite-difference code which ignored computation grids surrounded by the interior boundary to simulate flow around a rectangular cross section spur dike. However, the advantage disappears when it comes to non-rectangular cross section obstacles, such as circular bridge pier.

Immersed boundary (IB) method proposed by Peskin [6] has been widely used in the fluid–solid phase problem, such as prosthetic cardiac valve, swimming eels, sperm, and bacteria. IB method has also been used in many fixed-boundary fluid dynamics, such as flow around cylinder in two-dimensional domain (Lai and Peskin [7], Silva et al. [8], Su et al. [9]). Fadlun et al. [10] and Kim et al. [11] solved flow around complex geometric object in three-dimensional domain. Shen and Chan [12] used the IB method to simulate submerged solid bodies, and combined with volume of fluid (VOF) technique to simulate the interaction between free surface and submerged steps. Studies mentioned above verified the capability of IB methods by simulating the wake flow behind cylinder, and comparing the Strouhal number (dimensionless frequency of vortex shedding) or drag coefficient with that calculated experimentally.

In shallow-water flow domain, not the same as the fluid-dynamic cases mentioned previously, the Strouhal number is no longer the sufficient benchmark to justify the rationality of flow pattern. In this article, the comparison studies with experiments selected properly will be performed to examine the applicability of the IB method for shallow-water flow problems. The experiments from literatures include the round pier case deployed by Ahmed and Rajaratnam [13] and the spur dike case deployed by Rajaratnam and Nwachukwu [14]. The purpose to simulate the experiments is to justify the model's validity. Furthermore, hypothetical parallel-piers cases are designed to demonstrate the model's capability.

The IB method is commonly applied in the rectangular grid of Cartesian coordinate. To fit the boundary of natural rivers, the orthogonal curvilinear coordinate system is therefore used in this study to transfer the physical domain into the computational domain with rectangular grids, as shown in Fig. 1. This study demonstrates the applicability of the IB method and explores the advantages of using the IB method for shallow-water flow domain under orthogonal curvilinear coordinate.

* Corresponding author. Tel.: +886 3 5918542; fax: +886 3 5820017.
*E-mail address:* hsieh0812@itri.org.tw (T.-Y. Hsieh).

0045-7930/$ - see front matter © 2011 Elsevier Ltd. All rights reserved.
doi:10.1016/j.compfluid.2011.08.009

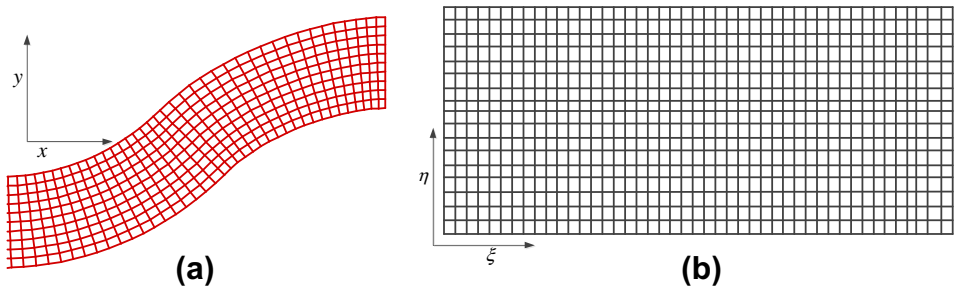


**Fig. 1.** Sketch of (a) physical domain and (b) computational domain.

## 2. Mathematical formulations

Following the concept of the IB method, the non-submerged obstacles in the flow field can be considered as a source of virtual force acting on the interior wall of obstacles. Its effect on the flow field is formulated as a source term in the momentum equation. The associated governing equations and solution formulation are described sequentially in the following.

### 2.1. Governing equations

This study follows the Warsi's [15] approach that the governing equations are transformed from the physical domain of Cartesian coordinate to the computational domain of orthogonal curvilinear coordinate. The governing equations are developed based on the assumptions including: (1) incompressible Newtonian fluid, (2) hydrostatic pressure distribution, (3) wind shear neglected at the water surface, (4) Coriolis acceleration ignored. The kinematic boundary conditions at the bed and the surface are applied to integrate Navier–Stokes equations to obtain 2-D depth-averaged shallow-water flow equations by Leibnitz rule (Hsieh and Yang [16], Miller and Chaudhry [17], Lin and Huang [18]). The governing equation with a virtual force term can be expressed in orthogonal curvilinear coordinate system as follows:

Continuity equation

$$h_1h_2\frac{\partial d}{\partial t}+\frac{\partial}{\partial\xi}(h_2Ud)+\frac{\partial}{\partial\eta}(h_1Vd)=0 \tag{1}$$

Momentum equations

$$\begin{aligned}&\frac{\partial U}{\partial t}+\frac{U}{h_1}\frac{\partial U}{\partial\xi}+\frac{V}{h_2}\frac{\partial U}{\partial\eta}+\frac{UV}{h_1h_2}\frac{\partial h_1}{\partial\eta}-\frac{V^2}{h_1h_2}\frac{\partial h_2}{\partial\xi}\\&=\frac{1}{\rho h_1h_2d}\frac{\partial}{\partial\xi}(h_2T_{11})+\frac{1}{\rho h_1h_2d}\frac{\partial}{\partial\eta}(h_1T_{12})+\frac{1}{\rho h_1h_2d}\frac{\partial h_1}{\partial\eta}T_{12}\\&\quad-\frac{1}{\rho h_1h_2d}\frac{\partial h_2}{\partial\xi}T_{22}+\frac{1}{\rho h_1h_2d}\left[-(h_2\tau_{11})_s\frac{\partial z_s}{\partial\xi}+(h_2\tau_{11})_b\frac{\partial z_b}{\partial\xi}\right.\\&\quad\left.-(h_1\tau_{12})_s\frac{\partial z_s}{\partial\eta}+(h_1\tau_{12})_b\frac{\partial z_b}{\partial\eta}\right]-\frac{g}{h_1}\frac{\partial}{\partial\xi}(d+z_b)-\frac{\tau_{b1}}{\rho d}+f(\xi)\end{aligned} \tag{2}$$

$$\begin{aligned}&\frac{\partial V}{\partial t}+\frac{U}{h_1}\frac{\partial V}{\partial\xi}+\frac{V}{h_2}\frac{\partial V}{\partial\eta}+\frac{UV}{h_1h_2}\frac{\partial h_2}{\partial\xi}-\frac{U^2}{h_1h_2}\frac{\partial h_1}{\partial\eta}\\&=\frac{1}{\rho h_1h_2d}\frac{\partial}{\partial\xi}(h_2T_{12})+\frac{1}{\rho h_1h_2d}\frac{\partial}{\partial\eta}(h_1T_{22})-\frac{1}{\rho h_1h_2d}\frac{\partial h_1}{\partial\eta}T_{11}\\&\quad+\frac{1}{\rho h_1h_2d}\frac{\partial h_2}{\partial\xi}T_{12}+\frac{1}{\rho h_1h_2d}\left[-(h_2\tau_{12})_s\frac{\partial z_s}{\partial\xi}+(h_2\tau_{12})_b\frac{\partial z_b}{\partial\xi}\right.\\&\quad\left.-(h_1\tau_{22})_s\frac{\partial z_s}{\partial\eta}+(h_1\tau_{22})_b\frac{\partial z_b}{\partial\eta}\right]-\frac{g}{h_2}\frac{\partial}{\partial\eta}(d+z_b)-\frac{\tau_{b2}}{\rho d}+f(\eta)\end{aligned} \tag{3}$$

in which,

$$T_{11}=\int_{z_b}^{z_s}[\tau_{11}-\rho\overline{u'^2}-\rho(\bar{u}-U)^2]dz \tag{4}$$

$$T_{22}=\int_{z_b}^{z_s}[\tau_{22}-\rho\overline{v'^2}-\rho(\bar{v}-V)^2]dz \tag{5}$$

$$T_{12}=T_{21}=\int_{z_b}^{z_s}[\tau_{12}-\rho\overline{u'v'}-\rho(\bar{u}-U)(\bar{v}-V)]dz \tag{6}$$

$$\frac{\tau_{11}}{\rho}-\overline{u'^2}=2\upsilon_t\left[\frac{1}{h_1}\frac{\partial\bar{u}}{\partial\xi}+\frac{\bar{v}}{h_1h_2}\frac{\partial h_1}{\partial\eta}\right] \tag{7}$$

$$\frac{\tau_{22}}{\rho}-\overline{v'^2}=2\upsilon_t\left[\frac{1}{h_2}\frac{\partial\bar{v}}{\partial\eta}+\frac{\bar{u}}{h_1h_2}\frac{\partial h_2}{\partial\xi}\right] \tag{8}$$

$$\frac{\tau_{12}}{\rho}-\overline{u'v'}=2\upsilon_t\left[\frac{h_2}{h_1}\frac{\partial}{\partial\xi}\left(\frac{\bar{v}}{h_2}\right)+\frac{h_1}{h_2}\frac{\partial}{\partial\eta}\left(\frac{\bar{u}}{h_1}\right)\right] \tag{9}$$

where $t$ is time; $\xi$ and $\eta$ are orthogonal curvilinear coordinates in streamwise axis and transverse axis, respectively; $h_1$ and $h_2$ are metric coefficients in $\xi$ and $\eta$ directions, respectively; $U$ and $V$ are the depth-averaged velocity components in $\xi$ and $\eta$ directions, respectively; $d$ is water depth; $\rho$ is fluid density; $g$ is gravitational acceleration; $z_b$ is bed elevation; $u$ and $v$ are velocity components in $\xi$ and $\eta$ directions, respectively; over bar ($\bar{}$) = time averaged; prime ($'$) = time fluctuating component; $T_{ij}$ = integrated effective stress; $\upsilon_t$ = turbulence kinematic viscosity = $ku_*d/6$ (Falconer [19]); $u_*=(\tau_b/\rho)^{1/2}$ = shear velocity; $k$ = von Karman's constant with a value of 0.4.

$\tau_{b1}$ and $\tau_{b2}$ are bottom shear stresses in $\xi$ and $\eta$ directions, respectively, modeled by Rastogi and Rodi [20] as follows

$$\tau_{b1}=c_f\rho U\sqrt{U^2+V^2} \tag{10}$$

$$\tau_{b2}=c_f\rho V\sqrt{U^2+V^2} \tag{11}$$

where $c_f=g/c^2$ = friction factor; $c$ = Chezy factor; $g$ = gravitational constant. The wind caused free surface shear stress is neglected, thus, $\tau_{s1}=0$ and $\tau_{s2}=0$.

In this model, the integrated effective stresses (Eqs. (4)–(6)) are treated with Boussinesq's eddy viscosity concept (Eqs. (7)–(9)). Although Lien et al. [21] and Miller and Chaudhry [17] show that the effective stresses can be ignored in straight channels, this study intends to maintain the integrity of numerical model, and hence the integrated effective stresses are not ignored. The integrated effective stresses are thereupon solved using an empirical profile which can be found in De Vriend [22] and Hsieh and Yang [16].

$f(\xi)$ and $f(\eta)$ in Eqs. (2) and (3) are the virtual forces of the IB method in $\xi$ and $\eta$ directions, respectively. The force is designed to enforce the proper boundary conditions on an arbitrary massless body that may or may not be coincided with the grid, as shown in

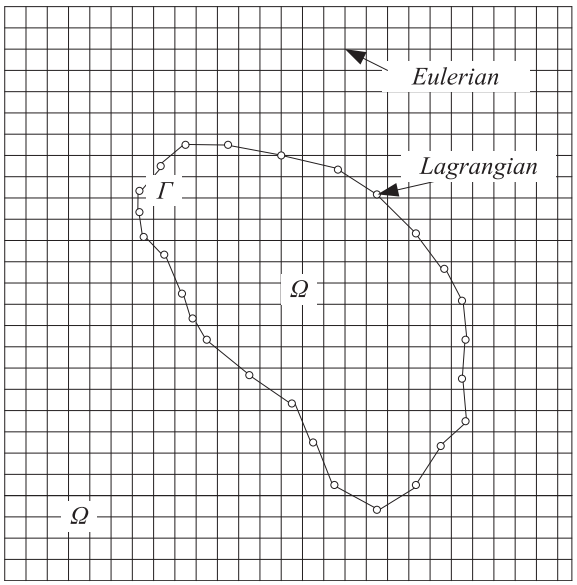


**Fig. 2.** Sketch of flow domain $\Omega$ and immersed boundary $\Gamma$.

Fig. 2. The circles in Fig. 2 are the markers in Lagrangian coordinate ($\Gamma$), used to describe the wall of boundary; $\Omega$ is the domain of flow, also known as the Eulerian grid.

### 2.2. Boundary conditions

Three types of boundary conditions including inlet, outlet, and both sides of wall are taken into account. The inlet boundary uses the unit-width discharge, and the outlet boundary uses the water surface elevation. In side wall, the boundary is set by the law of the wall (Nezu and Nakagawa [23]):

$$\frac{u_w}{U_*} = \frac{1}{\kappa}\ln\left(9\frac{y_w U_*}{\upsilon}\right) \tag{12}$$

$u_w$ = depth-averaged velocity nearing the wall; $y_w$ = distance between wall and nearing grid; $U_*$ = shear velocity = $(\tau_{b1}/\rho)^{1/2}$; $\kappa$ = von Karman's constant = 0.4; $\upsilon$ = kinematic viscosity.

### 2.3. Solution formulation for virtual force term

Fig. 2 demonstrates that the interior boundary of Eulerian domain is discretized by the IB markers which may not coincide with a grid. Therefore, the boundary condition, such as no slip condition, on the IB markers must be fulfilled first, and then be redistributed to grid. Mittal and Iaccarino [24] investigated various IB methods and categorized the methods that solve the interior boundary condition into two approaches: continue forcing and discrete forcing approaches. The advantages of first approach are simple and straightforward for implementation; the second one has the advantages in stability and applicability. Su et al. [9] developed a methodology that may achieve most advantages of both approaches simultaneously. In which, the IB method that solves a banded matrix is formulated from the geometric relations between the Eulerian grids and the Lagrangian markers with the non-slip boundary condition. The banded matrix can be expressed as a system of linear algebra equation as follows:

$$\begin{aligned} &A_{kj}\cdot F(\xi^k) = B_{1k} \\ &A_{kj}\cdot F(\eta^k) = B_{2k} \\ &k = \{1, M\}, j = \{1, M\} \end{aligned} \tag{13}$$

$F(\xi^k)$ and $F(\eta^k)$ represent the virtual forces on markers $k$ in $\xi$ and $\eta$ directions, respectively; $M$ = numbers of markers; $A_{kj}$ is the geometric relations between markers and grids, and the form of the relations are the same in $\xi$ and $\eta$ directions. $A_{kj}$ can be expressed as follows:

$$A_{kj} = \sum_{j=1}^{M}\left[\sum^{\Omega}\delta_h^k \Delta s^k \delta_h^j h_1 h_2\right] \tag{14}$$

$\Delta s^k$ is the averaged distance of one marker $k$ to neighboring two markers, that is $\Delta s^k = 0.5(\overline{s^{k+1}s^k} + \overline{s^k s^{k-1}})$, $s^k$ is the position of marker $k$; $\bar{}$ represents distance between the neighboring markers; $\delta_h^k$ represents $\delta_h$ (Dirac delta function) of marker $k$, which is a weighting function based on space distance, and will be described in Eqs. (18)–(20).

$B_{1k}$ and $B_{2k}$ are the velocity variations on markers $k$ in $\xi$ and $\eta$ directions, respectively, which can be expressed as follows:

$$\begin{aligned} B_{1k} &= \left[\frac{U^{*k} - U^k}{\Delta t}\right] \\ B_{2k} &= \left[\frac{V^{*k} - V^k}{\Delta t}\right] \end{aligned} \tag{15}$$

in Eq. (15), $U^{*k}$ and $V^{*k}$ represent the known velocity on markers; $U^k$ and $V^k$ mean the current velocities on markers. The known velocity should remain zero for static obstacles, and are equal to moving velocity for moving obstacles. The current velocities are calculated by Eqs. (1)–(3) and can be transformed from depth-averaged velocity, $U$ and $V$, by $\delta_h$ function as follows:

$$\begin{aligned} U^k &= \sum^{\Omega} U\delta_h^k \Delta s^k \\ V^k &= \sum^{\Omega} V\delta_h^k \Delta s^k \end{aligned} \tag{16}$$

To close Eqs. (2) and (3), the virtual forces, $F(\xi^k)$ and $F(\eta^k)$, on the IB markers need to be transformed into $f(\xi)$ and $f(\eta)$ on Eulerian grid. The transformation relations can be expressed as follows:

$$\begin{aligned} f(\xi) &= \sum_{k=1}^{M} F(\xi^k)\delta_h^k \Delta s^k \\ f(\eta) &= \sum_{k=1}^{M} F(\eta^k)\delta_h^k \Delta s^k \end{aligned} \tag{17}$$

From Eqs. (16) and (17), one can find that the key concept of $\delta_h$ function is used to redistribute the velocity and force between the Lagrangian and the Eulerian coordinates. Peskin [25] shows that the $\delta_h$ function can derived by 4 or 6 points. So far several methods including 2-point, 4-point and 6-point $\delta_h$ functions have been commonly used in computational fluid dynamics. However, Shin et al. [26] shows that the 6-point $\delta_h$ function might yield less stable results than others with less points. Therefore, the 4-point $\delta_h$ function and 2-point $\delta_h$ function are adopted in this study. The $\delta_h$ function can be calculated by the distribution function $d_h$ as follows:

$$\delta_h^k = d_h(\xi - \xi^k)d_h(\eta - \eta^k) \tag{18}$$

The 4-point $\delta_h$ function was presented by Lai and Peskin [7], and $d_h$ is calculated as follows:

$$d_h(r) = \begin{cases} \frac{1}{8\Delta h}\left(3 - 2\frac{r}{\Delta h} + \sqrt{1 + 4\frac{r}{\Delta h} - 4\left(\frac{r}{\Delta h}\right)^2}\right), & \text{for } |r| \leqslant \Delta h \\ \frac{1}{8\Delta h}\left(5 - 2\frac{r}{\Delta h} - \sqrt{-7 + 12\frac{r}{\Delta h} - 4\left(\frac{r}{\Delta h}\right)^2}\right), & \text{for } |r| \leqslant 2\Delta h \\ 0, & \text{otherwise} \end{cases} \tag{19}$$

where $r$ is $\xi - \xi^k$ or $\eta - \eta^k$, and $\Delta h$ is the grid size, equal to $\Delta\xi$ or $\Delta\eta$.

The 2-point $\delta_h$ function was presented by Su et al. [9], and $d_h$ can be represented as follows:

$$d_h(r) = \begin{cases} \left(1 - \frac{|r|}{\Delta h}\right)\frac{1}{\Delta h}, & \text{for} |r| \leqslant \Delta h \\ 0, & \text{otherwise} \end{cases} \tag{20}$$

In this study, both 4-point and 2-point $\delta_h$ functions are conducted to demonstrate their capability and distinction as applied to shallow-water flow computation.

## 3. Numerical methodology

### 3.1. Operator-splitting approach

The finite difference method is employed to discretize the governing equations. The operator-splitting approach proposed by Hsieh and Yang [16] is used to solve the governing equations. The first step (dispersion process) takes into account the advection terms and diffusion terms in the momentum equations to compute the provisional velocity. The second step (propagation process) solves the water depth by computing the pressure and bed friction terms of Eqs. (2) and (3), and the continuity equation, and then corrects the provisional velocity. The third step is to correct the velocity by solving the virtual force term. The first-order forward differencing is used for time derivative, and the numerical scheme for the spatial derivative terms will be introduced in Section 3.2. The following is the difference form of the operator-splitting approach.

Dispersion step

$$\begin{aligned} &\frac{U^{n+1/2} - U^n}{\Delta t} + \frac{U^n}{h_1}\frac{\partial U^{n+1/2}}{\partial \xi} + \frac{V^n}{h_2}\frac{\partial U^{n+1/2}}{\partial \eta} + \frac{U^n V^n}{h_1 h_2}\frac{\partial h_1}{\partial \eta} - \frac{(V^n)^2}{h_1 h_2} \\ &\quad \times \frac{\partial h_2}{\partial \xi} \\ &= \frac{1}{\rho h_1 h_2 d^n}\left[\frac{\partial (h_2 T_{11}^{n+1/2})}{\partial \xi} + \frac{\partial (h_1 T_{12}^{n+1/2})}{\partial \eta} + \frac{\partial h_1}{\partial \eta} T_{12}^{n+1/2} - \frac{\partial h_2}{\partial \xi} T_{22}^{n+1/2}\right] \\ &\quad + \frac{1}{\rho h_1 h_2 d^n}\left[-(h_2 \tau_{11})_s^n \frac{\partial z_s^n}{\partial \xi} + (h_2 \tau_{11})_b^n \frac{\partial z_b^n}{\partial \xi} - (h_1 \tau_{12})_s^n \frac{\partial z_s^n}{\partial \eta}\right. \\ &\quad \left. + (h_1 \tau_{12})_b^n \frac{\partial z_b^n}{\partial \eta}\right] \end{aligned} \tag{21}$$

$$\begin{aligned} &\frac{V^{n+1/2} - V^n}{\Delta t} + \frac{U^n}{h_1}\frac{\partial V^{n+1/2}}{\partial \xi} + \frac{V^n}{h_2}\frac{\partial V^{n+1/2}}{\partial \eta} + \frac{U^n V^n}{h_1 h_2}\frac{\partial h_2}{\partial \xi} - \frac{(U^n)^2}{h_1 h_2} \\ &\quad \times \frac{\partial h_1}{\partial \eta} \\ &= \frac{1}{\rho h_1 h_2 d^n}\left[\frac{\partial (h_2 T_{12})^{n+1/2}}{\partial \xi} + \frac{\partial (h_1 T_{22})^{n+1/2}}{\partial \eta} - \frac{\partial h_1}{\partial \eta} T_{11}^{n+1/2} + \frac{\partial h_2}{\partial \xi} T_{12}^{n+1/2}\right] \\ &\quad + \frac{1}{\rho h_1 h_2 d^n}\left[-(h_2 \tau_{12})_s^n \frac{\partial z_s^n}{\partial \xi} + (h_2 \tau_{12})_b^n \frac{\partial z_b^n}{\partial \xi} - (h_1 \tau_{22})_s^n \frac{\partial z_s^n}{\partial \eta}\right. \\ &\quad \left. + (h_1 \tau_{22})_b^n \frac{\partial z_b^n}{\partial \eta}\right] \end{aligned} \tag{22}$$

where the superscript $(n + 1/2)$ represents the variable determined by the dispersion step $(n + 1/2)$, and the superscript $n$ represents a known variable at time step $(n)$.

Propagation step

$$\frac{U^p - U^{n+1/2}}{\Delta t} = -\frac{g}{h_1}\left[\frac{\partial (z_b + d)^{n+1}}{\partial \xi}\right] - \frac{c_f U^p \sqrt{(U^{n+1/2})^2 + (V^{n+1/2})^2}}{d^n} \tag{23}$$

$$\frac{V^p - V^{n+1/2}}{\Delta t} = -\frac{g}{h_2}\left[\frac{\partial (z_b + d)^{n+1}}{\partial \eta}\right] - \frac{c_f V^p \sqrt{(U^{n+1/2})^2 + (V^{n+1/2})^2}}{d^n} \tag{24}$$

$$h_1 h_2 \frac{d^{n+1} - d^n}{\Delta t} + \frac{\partial}{\partial \xi}(h_2 U^p d^{n+1}) + \frac{\partial}{\partial \eta}(h_1 V^p d^{n+1}) = 0 \tag{25}$$

where the superscript $p$ means variables of propagation step being determined, the superscript $(n + 1)$ denotes the unknown variables at time step $(n + 1)$. Eqs. (23)–(25) are combined to linearize the depth in $n + 1$ time step; and hence, the depth increment equation can be derived. The propagation velocity can be rearranged from Eqs. (23) and (24) as follows:

$$\begin{aligned} U^p &= \frac{1}{C_\tau} U^{n+1/2} - \frac{g\Delta t}{C_\tau h_1}\left[\frac{\partial z_b}{\partial \xi} + \frac{\partial d^{n+1}}{\partial \xi}\right] \\ V^p &= \frac{1}{C_\tau} V^{n+1/2} - \frac{g\Delta t}{C_\tau h_2}\left[\frac{\partial z_b}{\partial \eta} + \frac{\partial d^{n+1}}{\partial \eta}\right] \end{aligned} \tag{26}$$

$$C_\tau = 1 + \Delta t \frac{c_f \sqrt{(U^{n+1/2})^2 + (V^{n+1/2})^2}}{d^n} \tag{27}$$

Using Taylor series expansion for the water depth, $d^{n+1}$, remaining the first order terms, and using $\Delta d = d^{n+1} - d^n$ as depth increment, Eq. (26) can be linearized as follows:

$$\begin{aligned} h_2 U^p d^{n+1} &= \alpha_1 \frac{\partial (\Delta d)}{\partial \xi} + \beta_1 \Delta d + \gamma_1 \\ h_1 V^p d^{n+1} &= \alpha_2 \frac{\partial (\Delta d)}{\partial \eta} + \beta_2 \Delta d + \gamma_2 \end{aligned} \tag{28}$$

where

$$\alpha_1 = -\frac{h_2 g \Delta t}{C_\tau h_1} d^n, \quad \beta_1 = \frac{h_2}{C_\tau} U^{n+1/2} - \frac{h_2 g \Delta t}{C_\tau h_1}\left[\frac{\partial z_b}{\partial \xi} + \frac{\partial d^n}{\partial \xi}\right], \quad \gamma_1 = \beta_1 d^n$$

$$\alpha_2 = -\frac{h_1 g \Delta t}{C_\tau h_2} d^n, \quad \beta_2 = \frac{h_1}{C_\tau} V^{n+1/2} - \frac{h_1 g \Delta t}{C_\tau h_2}\left[\frac{\partial z_b}{\partial \eta} + \frac{\partial d^n}{\partial \eta}\right], \quad \gamma_2 = \beta_2 d^n$$

Substituting Eq. (28) into Eq. (25) one can obtain the depth increment equation

$$\begin{aligned} &h_1 h_2 \frac{\Delta d}{\Delta t} + \frac{\partial}{\partial \xi}\left(\alpha_1 \frac{\partial (\Delta d)}{\partial \xi} + \beta_1 \Delta d + \gamma_1\right) \\ &\quad + \frac{\partial}{\partial \eta}\left(\alpha_2 \frac{\partial (\Delta d)}{\partial \eta} + \beta_2 \Delta d + \gamma_2\right) \\ &\quad = 0 \end{aligned} \tag{29}$$

and Correction step

$$\frac{U^{n+1} - U^p}{\Delta t} = f(\xi), \quad \frac{V^{n+1} - V^p}{\Delta t} = f(\eta) \tag{30}$$

The virtual force terms in $\xi$ and $\eta$ directions are solved implicitly in Eqs. (13) and (17), to exhibit the influence induced by the interior obstacle to the flow domain.

### 3.2. Numerical scheme

The advection terms in Eqs. (21) and (22) are discretized implicitly by a hybrid scheme (Lien et al. [21]). The hybrid scheme combines the upwind and central difference schemes to capture the flow direction. It can be expressed as follows:

$$\frac{U^n}{h_1}\left(\frac{\partial\varphi^{n+1/2}}{\partial\xi}\right)=0.5\frac{U^n_{ij}}{h_{1_{ij}}}\left[(1-\alpha_x)\left(\frac{\varphi^{n+1/2}_{i+1j}-\varphi^{n+1/2}_{ij}}{\Delta\xi}\right)+(1+\alpha_x)\left(\frac{\varphi^{n+1/2}_{ij}-\varphi^{n+1/2}_{i-1j}}{\Delta\xi}\right)\right] \tag{31}$$

$$\frac{V^n}{h_2}\left(\frac{\partial\varphi^{n+1/2}}{\partial\eta}\right)=0.5\frac{V^n_{ij}}{h_{2_{ij}}}\left[(1-\alpha_y)\left(\frac{\varphi^{n+1/2}_{ij+1}-\varphi^{n+1/2}_{ij}}{\Delta\eta}\right)+(1+\alpha_y)\left(\frac{\varphi^{n+1/2}_{ij}-\varphi^{n+1/2}_{ij-1}}{\Delta\eta}\right)\right] \tag{32}$$

where $\varphi$ can be $U$ or $V$;

$$\alpha_x=\begin{cases}0 & |R_x|\leqslant 2\\ 1 & R_x>2\\ -1 & R_x<-2\end{cases},\quad \alpha_y=\begin{cases}0 & |R_y|\leqslant 2\\ 1 & R_y>2\\ -1 & R_y<-2\end{cases},$$

where $R_x=\frac{U^n_{ij}h_{1ij}\Delta\xi}{\mu/\rho}$ and $R_y=\frac{V^n_{ij}h_{2ij}\Delta\eta}{\mu/\rho}$ are the mesh Reynolds number for $\xi$ and $\eta$ directions, respectively, and $\mu$ = dynamic viscosity. In the above scheme, the central difference scheme is used for the low mesh Reynolds number, whereas the upwind scheme is used for the high mesh Reynolds number. One can note that the mesh Reynolds number and the dynamic viscosity are the numerical parameters used to determine the suitable numerical method; and both the parameters are not related to the governing equations.

The rest terms of Eqs. (21), (22), and (29) are solved using control-volume concept and discretized by the central difference scheme, which can be expressed as follows:

$$\left(\frac{\partial\Psi}{\partial\xi}\right)^{n+1}_p=\frac{\Psi^{n+1}_e-\Psi^{n+1}_w}{\Delta\xi},\quad \left(\frac{\partial\Psi}{\partial\eta}\right)^{n+1}_p=\frac{\Psi^{n+1}_n-\Psi^{n+1}_s}{\Delta\eta} \tag{33}$$

where $\Psi$ can be $U$, $V$ or $d$, $\Psi_e=0.5(\Psi_{i+1j}+\Psi_{ij})$, $\Psi_w=0.5(\Psi_{ij}+\Psi_{i-1j})$, $\Psi_n=0.5(\Psi_{ij+1}+\Psi_{ij})$, and $\Psi_s=0.5(\Psi_{ij}+\Psi_{ij-1})$.

### 3.3. Solution procedure

The solution procedure for solving the discretized governing equations expressed previously can be summarized as follows:

1. Calculate the provisional velocities ($U^{n+1/2}$, $V^{n+1/2}$) implicitly by the alternating direction implicit (ADI) method from Eqs. (21) and (22) without the pressure gradient terms and friction terms.
2. Compute Eq. (29) implicitly to obtain depth at time $n+1$ by the ADI method.
3. The velocities ($U^p$, $V^p$) are calculated to correct the provisional velocities with the pressure gradient and bed friction from Eq. (26) to complete the propagation step.
4. Use Eq. (13) to calculate $F(\xi^k)$ and $F(\eta^k)$, and then Eq. (17) is used to calculate $f(\xi)$ and $f(\eta)$.
5. Use Eq. (30) to obtain velocity at time $n+1$ around interior boundary.
6. Repeat procedures 1–5 until a steady state solution is reached (for steady flows) or the specific time period is completed (for unsteady flows).

## 4. Examination on model's accuracy and stability

From the mathematical formulation as described previously, one can justify that the model's accuracy is closely related to the parameters introduced by using the IB method, which include the marker's mesh width distribution and the grid size. To evaluate the effects of parameters variation to the model accuracy, several test cases are designed for each parameter varied with sufficient wide range, and the discrepancy between simulation results and experimental data are calculated and analyzed. Both the 4-point and 2-point $\delta_h$ functions are adopted for each test case to demonstrate the influence from the different $\delta_h$ function to the flow field accuracy.

The single pier experiment, known as the C2R case, carried out by Ahmed and Rajaratnam [13] is adopted in this study. The layout of the channel and the pier geometry for the experiment is shown in Fig. 3. The horizontal flume is 20 m long and 1.22 m wide. The pier is located at 13 m from upstream. The inflow discharge is 0.065 cms and the depth is 0.182 m. The roughness is calculated by Manning's formula, $n=d_m^{1/6}/21.1$ (Henderson [27]), where $d_m$ = mean diameter of particle size which is 1.84 mm for the sand glued on wooden plank in the experiment. The Froude number ($F_r=U/\sqrt{gd}$) is 0.22 and the Reynolds number ($R_e=\rho U\ell/\mu$, where $\ell$ = diameter of pier or length of spur dike) is 24,800.

The $\delta_h$ function used for the virtual force computation which is related to the distance between the marker and grid implicitly indicates that the model's accuracy may be affected by the various conjunctive selections of marker distributions and coordinate grids. To justify their respective effect, first of all the model's accuracy in terms of velocity variation will be examined to evaluate the influence of various marker distributions with a constant grid size, and the effect of varied grid sizes with representative constant marker's mesh width.

In the study, RMS error is used as an index to present the discrepancy of velocity between the numerical simulation and experimental data, stated as follows:

$$\text{RMS error}=\sqrt{\frac{\sum_{i=1}^{N}(x_i-y_i)^2}{N}} \tag{34}$$

where $x_i$ and $y_i$ represent the experimental and simulation velocity, respectively; and $N$ represents the number of data at different positions. In this study, the RMS error is only evaluated at the same position where the velocity is measured in the experiment, as shown in Fig. 3. One of the positions measured is represented by the black line, in Fig. 3, on one side of the pier with a distance being three times the radius of the pier, along upstream to downstream of the pier. The other one is located in front of the pier with the distance being five times the radius of the pier, along the center of the channel to the left side wall.

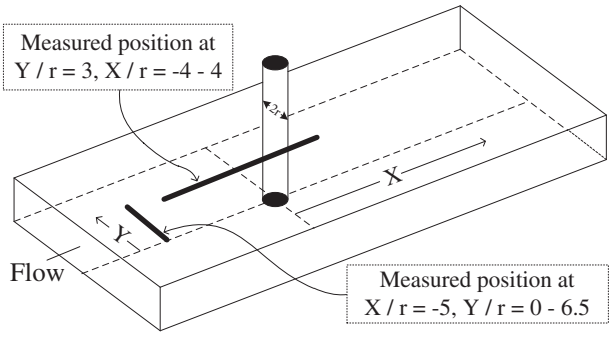


**Fig. 3.** Layout of experiment for flow passing through a single pier (Ahmed and Rajaratnam [13]).

### 4.1. Marker's mesh width effect

The marker can be uniformly or non-uniformly distributed, whereas the later fits the real case better as far as the natural complex geometry concerned. In the following, the uniform marker distribution is evaluated first. Fig. 4 shows the variation of RMS errors with respect to the ratio of marker's mesh width to the grid size, $\Phi = \Delta s/\Delta\eta$, for the cases simulated by the 4-point and 2-point $\delta_h$ functions with uniform grid. In which, $\Delta\xi = \Delta\eta = 0.002$ m is adopted. For the cases studied here, one can find that taking into account the model's stability, the value of $\Phi$ cannot be approximately less than the critical value of 0.6 for the 2-point $\delta_h$ function, and 0.7 for the 4-point $\delta_h$ function. Below the critical value it may cause singular solution in the system of linear algebra of Eq. (13). On the other hand, as $\Phi$ is greater than 2.0, the virtual force might be underestimated using the 2-point $\delta_h$ function, as shown in Fig. 4, where the RMS error increases rapidly.

However, for most range of $\Phi$ the results show that the RMS errors are well confined, even with the value of $\Phi$ being as large as 2.5, the RMS error for the 2-point $\delta_h$ function is still quite small (around 0.02). The case simulated here indicates that the result accuracy by the proposed IB model highly resonates the experimental results under the conditions of uniform marker distribution, uniform grid size of 0.002 m, and $\Phi < 2.5$, no matter which $\delta_h$ function is used.

To evaluate the effect due to the non-uniformity of marker distributions, cases with various $\Phi$ marker distributions around the pier are investigated. The conceptual sketch of marker distributions with $\Phi$ values of 1.8 and 1.0 are shown in Fig. 5; in which, $\Phi = 1.8$ is used to distribute the markers along the left hand side of the pier boundary, whereas $\Phi = 1.0$ is for the right hand side. The test cases include those with starting angle $\theta = 30°$ and with increment of 20° till reaching $\theta = 330°$. Fig. 6 shows the results of velocity RMS errors with respect to various angle of $\theta$, which are computed from the 2-point and 4-point $\delta_h$ functions, respectively.

RMS errors on both sides of the pier are presented to examine how the non-uniform distribution of the marker's mesh width affects the velocity field around the pier. From Fig. 6, the results given by the 2-point $\delta_h$ function show no systematic RMS error along two sides of the pier. On the contrary, the results given by the 4-point $\delta_h$ function show consistently systematic fluctuations being confined in a very small range with considerably same values. This may indicate that the flow field along both sides conserves the symmetric pattern presents less sensitivity to the marker's non-uniformity.

### 4.2. Grid size effect

The grid size effect will be analyzed on the basis of two categories including the uniform grid with grid aspect ratio ($\Delta\xi/\Delta\eta$)

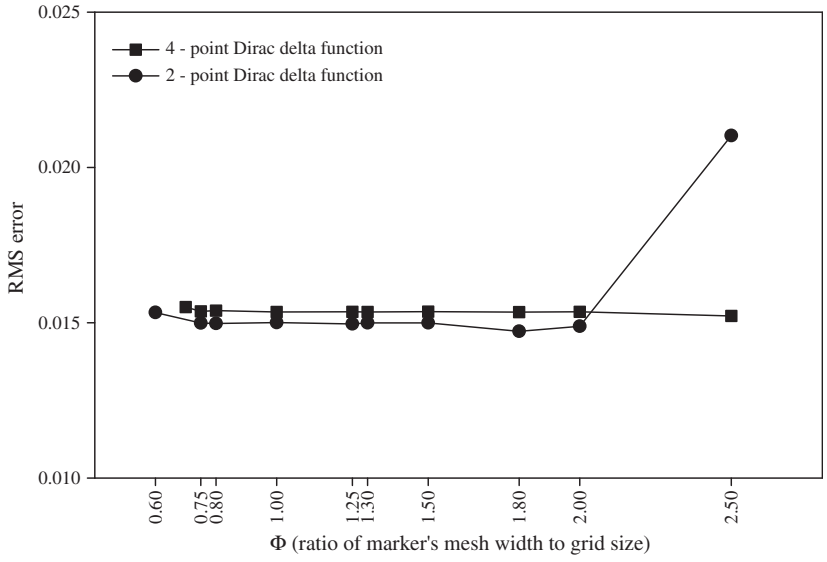


**Fig. 4.** RMS error between simulation and experimental data with respect to $\Phi$.

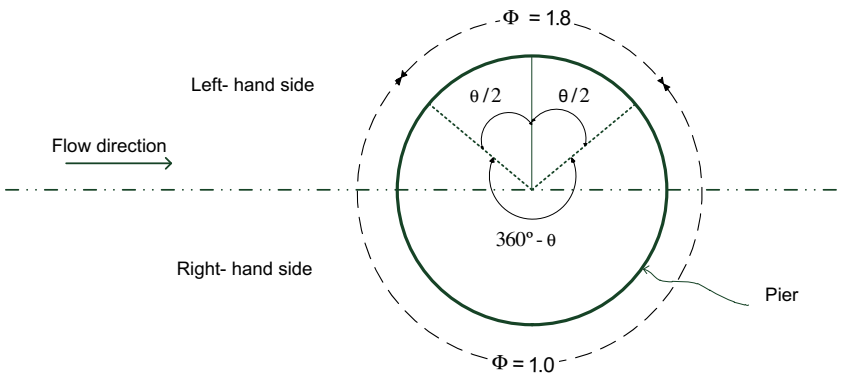


**Fig. 5.** Sketch of non-uniform marker's distribution with $\Phi$ varying around the pier.

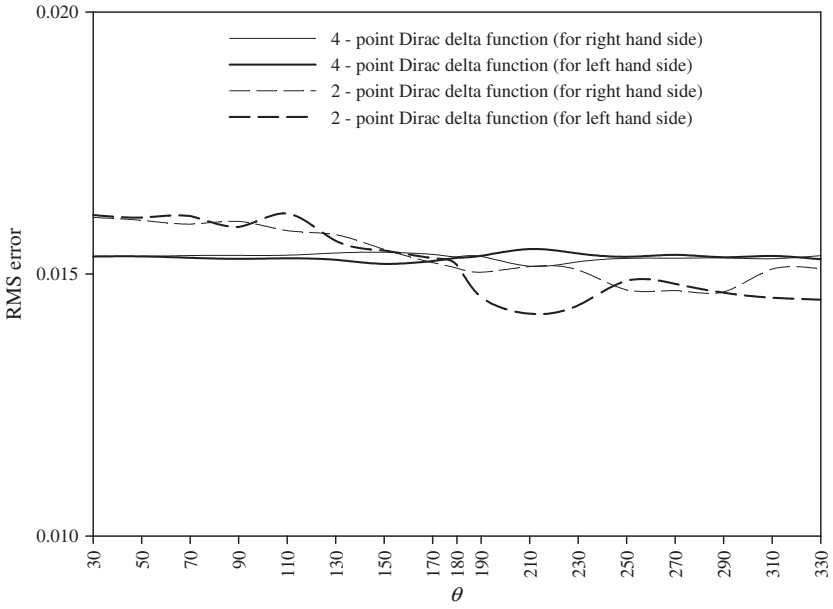


**Fig. 6.** Variation of RMS error with respect to $\theta$.

**Table 1**
List of numerical parameters for grid size test.

| Test cases | Grid size (m) | Grid aspect ratio |
|---|---|---|
| Uniform grid cases | 0.0005, 0.001, 0.002, 0.003, 0.005, 0.01, 0.015, 0.02 | 1 |
| Non-uniform grid cases | Grid size in $\eta$ direction is fixed as 0.002 | 0.05, 0.2, 0.5, 1.0, 1.5, 2.0, 5.0 |

equal to unity and non-uniform grid with various grid aspect ratios, whereas the grid size in $\eta$ direction is fixed as $\Delta\eta = 0.002$. The designed cases are listed in Table 1. The markers are deployed uniformly to simplify the analysis on the marker's mesh width effect. $\Phi = 0.6$ and 0.7 are adopted in these tests because they are the smallest critical value allowed in terms of model stability for the 2-point and 4-point $\delta_h$ functions, respectively, being pointed out previously from the outcome shown in Fig. 4.

Cases with uniform grid sizes including – 0.0005 m, 0.001 m, 0.002 m, 0.003 m, 0.005 m, 0.01 m, 0.015 m, and 0.02 m – are used to examine the influence of grid size on the model accuracy in comparison to the experiment. Fig. 7 depicts the RMS errors varies with respect to the grid sizes. One can find that the discrepancy becomes more significant with coarser grid sizes. The RMS error varies in the range from 0.015 to 0.03. The influence of the grid size on the model accuracy becomes less with the grid size finer than 0.005 m; and the error reduces about 50% in comparison to that with the grid size of 0.02 m. The difference is 0.15% between the two $\delta_h$ functions in average, which means both the $\delta_h$ functions behave similarly for the cases with uniform grids and uniform marker distributions.

For non-uniform grid cases with various grid aspect ratios, as mentioned previously a constant space interval in $\eta$ direction $\Delta\eta = 0.002$ m is used, and the space interval in $\xi$ direction, $\Delta\xi$ varies from 0.0001 m to 0.01 m, and therefore providing the grid aspect ratio ranging from 0.05 to 5.0. Herein the uniform marker's mesh width ($\Delta s$) is set up based on the grid space interval in $\eta$ direction, that is $\Delta s = \Phi_\eta \Delta\eta$, in which $\Phi_\eta = 0.6$ and 0.7 are adopted for the 2-point and 4-point $\delta_h$ functions, respectively.

Fig. 8 demonstrates the variation of RMS error with respect to various values of grid aspect ratio for the 2-point and 4-point $\delta_h$ functions. The RMS errors for cases with grid aspect ratio from 0.05 to 1.5, as shown in Fig. 8, vary from 0.022 to 0.013. As grid aspect ratio equal to unity, cases from both the 2-point and 4-point $\delta_h$ functions show the least RMS discrepancy, and the simulation shows insignificant difference between the two $\delta_h$ functions. For cases with the grid aspect ratio >1.5, the simulation results are unstable and cannot be accomplished, since the $\Phi_\zeta(\Delta s/\Delta\zeta))$ is below the critical values of 0.6 or 0.7 as discussed previously based on the results shown in Fig. 4.

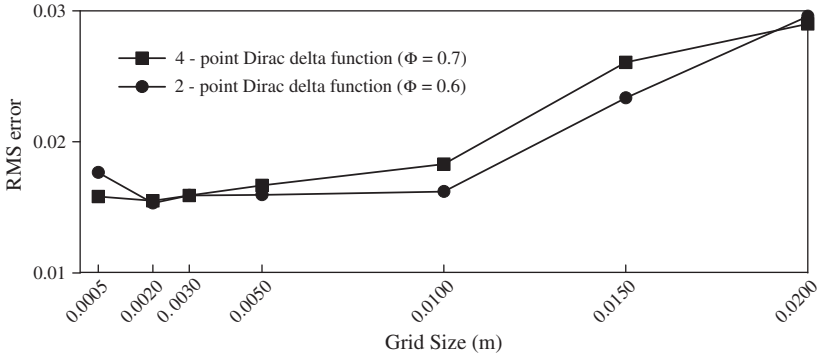


**Fig. 7.** Variation of RMS error with respect to grid size.

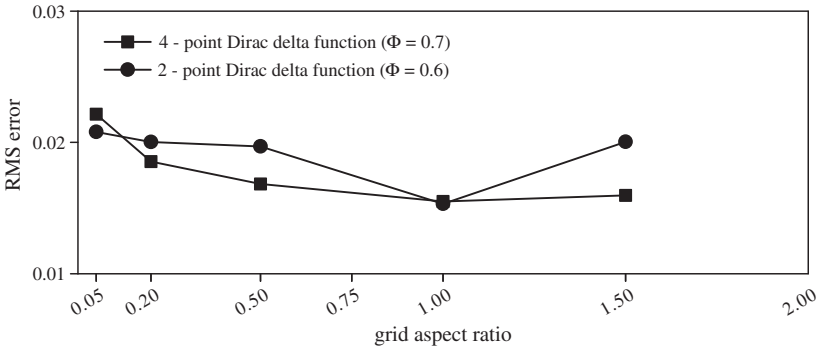


**Fig. 8.** Variation of RMS error with respect to grid aspect ratio.

## 5. Examination on Dirac delta function

From the results of previous studies, the proposed model can approximate the experimental data well and keep the error in an acceptable range under certain conditions as discussed above. Su et al. [9] indicated that the 2-point $\delta_h$ function can give considerably sufficient accuracy for their test cases under the condition of Strouhal number or drag coefficient effects. To further examine the pro/con of the 2-point and 4-point $\delta_h$ functions for shallow-water flow, the test analysis based on various Froude numbers for the C2R experiment by Ahmed and Rajaratnam [13] is carried out subsequently. The test cases are studied under the conditions of a marker distribution with $\Phi = 1.0$, grid aspect ratio = 1.0, and grid size = 0.002 m.

Following the experiment layout in Fig. 3, Fig. 9 shows the variation of dimensionless velocity at the position of $Y/r = 3$ along the channel reach from upstream point, $X/r = -4$ to downstream point, $X/r = 4$. The dimensionless velocity = $w/U_0$, where $w = (U^2 + V^2)^{1/2}$ and $U_0$ is upstream free-stream velocity. Fig. 10 shows the distribution of dimensionless velocity for the cross section at the position

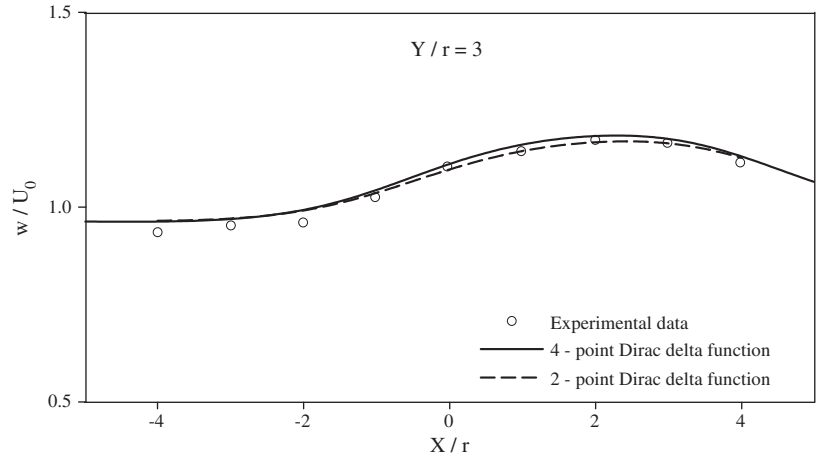


**Fig. 9.** Simulated and experimental dimensionless velocity at $Y/r = 3$ with different $\delta_h$ functions along the longitudinal dimensionless distance.

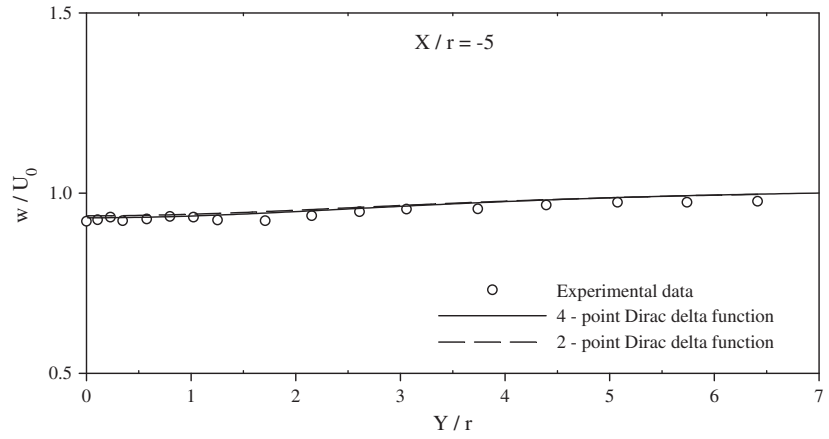


**Fig. 10.** Simulated and experimental dimensionless velocity at $X/r = -5$ with different $\delta_h$ functions along the lateral dimensionless distance.

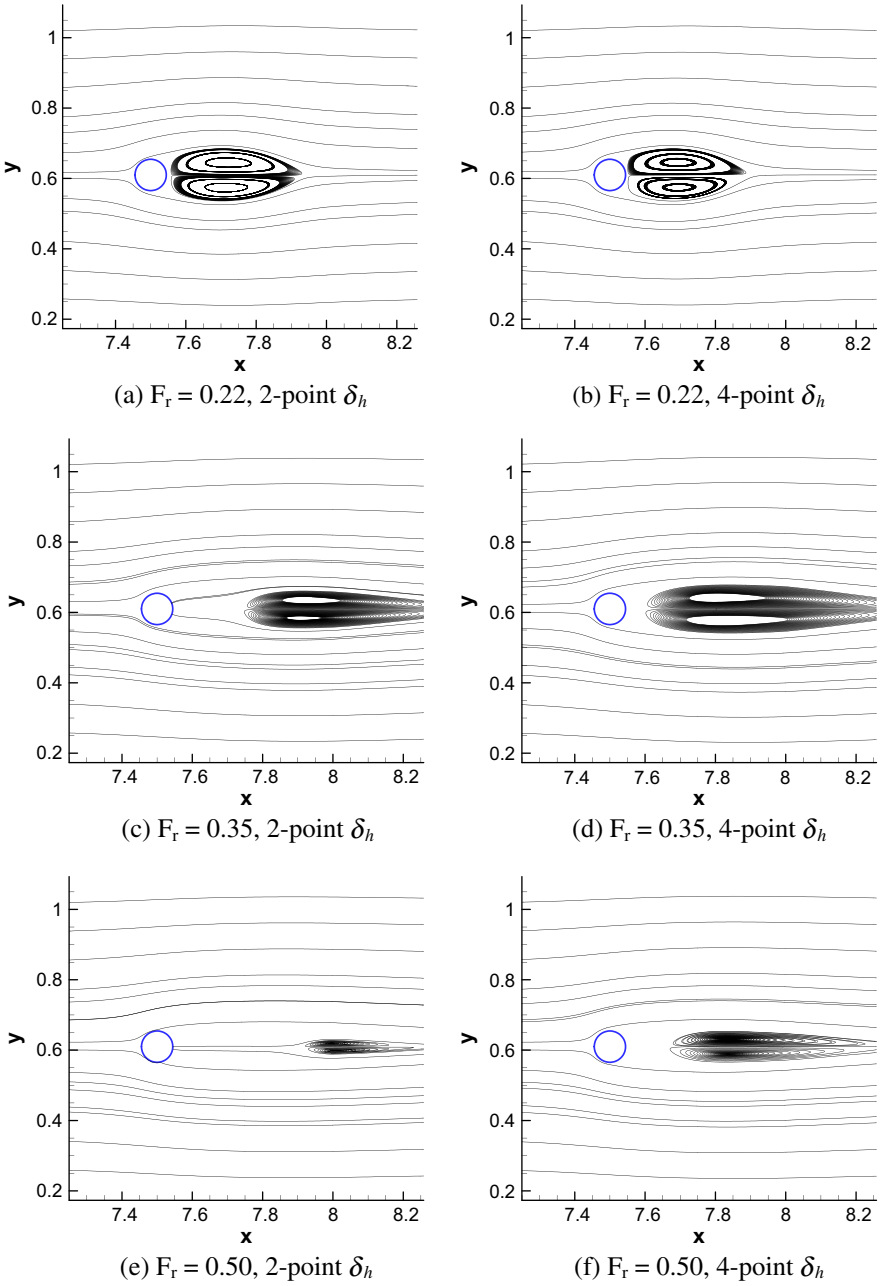


(a) $F_r = 0.22$, 2-point $\delta_h$ (b) $F_r = 0.22$, 4-point $\delta_h$

(c) $F_r = 0.35$, 2-point $\delta_h$ (d) $F_r = 0.35$, 4-point $\delta_h$

(e) $F_r = 0.50$, 2-point $\delta_h$ (f) $F_r = 0.50$, 4-point $\delta_h$

**Fig. 11.** Configurations of simulated stream line with use of different $\delta_h$ for various Froude numbers.

of $X/r = -5$ from the center of channel to the side wall, which is nearly located right at upstream of pier. From Figs. 9 and 10, one can find that both the 2-point and 4-point $\delta_h$ functions give consistent results with the experimental data, except that the peak velocity from the 2-point $\delta_h$ function is less than that from the 4-point $\delta_h$ function as shown in Fig. 9.

From the above comparison, in fact, it is difficult to identify the pro/con of both the 2-point and 4-point $\delta_h$ functions. To further examine the inside details, the following additional hypothetical cases with larger Froude number are designed by steepening the slope of C2R case. The slope is steepened to 0.044% and 0.092% for which the Froude numbers are equal to 0.35 and 0.50, respectively; the Reynolds numbers are equal to 60,207 and 81,184, respectively; and parameters such as the marker distribution, grid aspect ratio and grid size are as same as mentioned previously.

Fig. 11 shows the configuration of stream line simulated using the 2-point and 4-point $\delta_h$ functions for the cases with Froude numbers equal to 0.22, 0.35 and 0.50. The results show that as the Froude number increases the vortex is being shed farther away from the pier. Under a same Froude number, the simulation results also demonstrate that vortex is shed farther from the pier by the 2-point $\delta_h$ function than that by the 4-point $\delta_h$ function. The intrinsic property of the IB method which allows the flow mass penetrating through immersed body may reveal some sort of interpretation about this phenomenon. For the cases studied here, one can find that the mass penetrating through the pier given by the 2-point $\delta_h$ function is greater than that given by the 4-point $\delta_h$ function, as shown in Table 2. Apparently, the 4-point $\delta_h$ function gives the better approximation in terms of the less mass loss through the pier.

**Table 2**
List of mass penetrating rate in terms of Dirac delta function and Froude numbers.

| Froude number | Mass penetrating rate (%) | |
|---|---|---|
| | 4-point $\delta_h$ function | 2-point $\delta_h$ function |
| 0.22 | 0.77 | 1.02 |
| 0.35 | 1.35 | 1.78 |
| 0.5 | 1.57 | 2.04 |

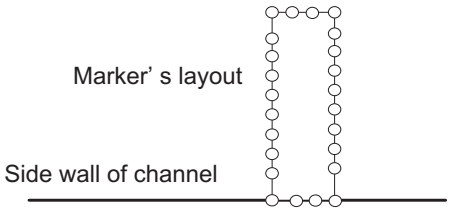


**Fig. 13.** Markers distributed around the spur dike wall.

## 6. Validation and application

As mentioned in previous studies, the 4-point $\delta_h$ function not only intensifies the grid size effect and marker's mesh width, but also performs more reasonable flow field as far as the mass conservation concerned at the condition with a larger Froude number. Therefore, the 4-point $\delta_h$ function is adopted for the following studies and further demonstrates the applicability of the IB method for shallow-water flow computation.

### 6.1. Model validation with spur dike case

Spur dike experiments by Rajaratnam and Nwachukwu [14] is simulated by the proposed model, and the measured velocity profile around the non-submerged spur dike is used to validate the simulation results. Fig. 12 shows the layout of the experiment, which is a uniform rectangular channel with a length of 37 m, a width of 0.9 m, a horizontal bed. The length of spur dike, $b$, is 0.152 m. Flow discharge at upstream boundary is steady and uniform, with value of 0.0446 $m^3/s$; downstream depth is 0.189 m; Froude number is 0.19; and Reynolds number is 46,944.

The grid size is 0.005 m and the grid aspect ratio is 1.0. The marker distribution is non-uniform along the boundary of spur dike, as shown in Fig. 13. $\Phi$ values ranges from 1.0 to 1.2; most of them are, in fact, equal to unity, except those along the corners which ranges from 1.1 to 1.2. The simulation results are compared with the experimental data which was measured in several positions. As shown in Fig. 12, in terms of flow direction, five groups of data located at $y/b$ equals to 1.0, 1.5, 2.0, 3.0 and 4.0 are measured. The data of groups at $y/b$ equal to 1.0 and 1.5 are measured from $x/b = -6$ to $x/b = 0$, and the other three groups are measured from $x/b = -6$ to $x/b = 8$.

Fig. 14 shows the variation of non-dimensionalized velocity, $w/U_0$, where $w = (U^2 + V^2)^{1/2}$ and $U_0$ is upstream free-stream velocity, at various locations along the distance $x/b$. The simulation results at $y/b = 1$ agree well with the experimental data. The velocity increases rapidly near the spur dike head, whereas the simulated velocity is slightly underestimated. The discrepancy appears owing that the markers are positioned along the boundary and not coincides with the measured positions. In which, the no-slip condition is needed to satisfy the IB method. From Fig. 14, one can observe that as the flow field is farther away from the spur dike, the simulation results approximate to the experimental ones, due to less non-slip boundary condition effect from the spur dike.

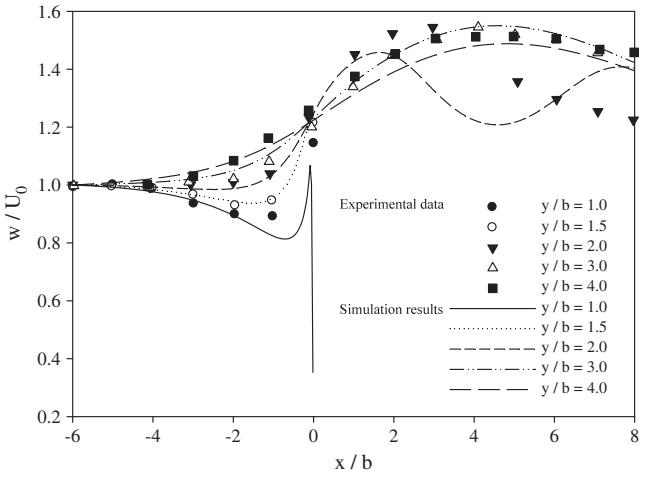


**Fig. 14.** Dimensionless velocity variation along the longitudinal direction at various $y/b$.

Along the computational points at $y/b \leqslant 2$ in flow direction, the simulation results for the upstream portion of the spur dike follow the trend of experimental data; but those for the downstream portion, the simulation result at $y/b = 2$ separates from the experimental data, and the peak value is, therefore, underestimated and out of phase.

### 6.2. Application to piers in parallel

The channel geometry and flow condition used in the following case is the same as the study by Ahmed and Rajaratnam [13] as described previously. Various numbers of piers are deployed in

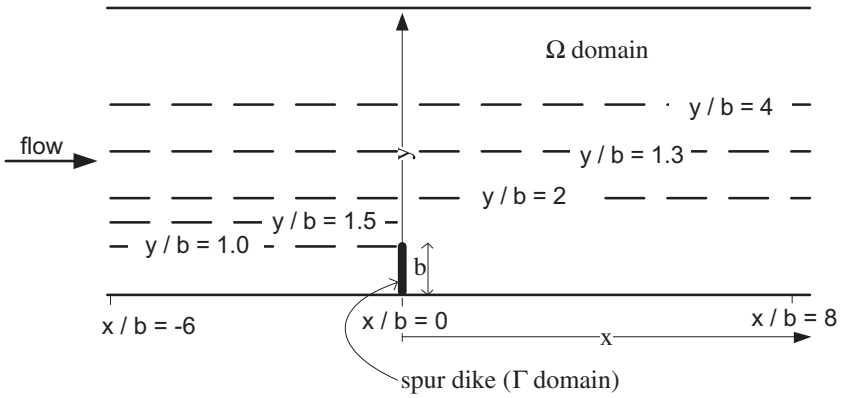


**Fig. 12.** Layout of spur dike in channel.

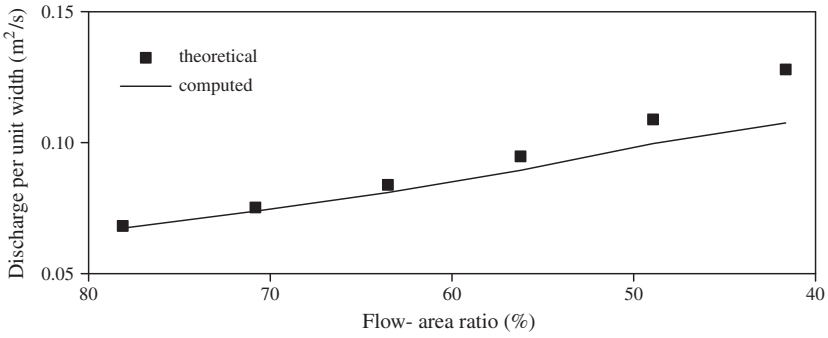


**Fig. 15.** Discharge per unit width with respect to variation of flow-area ratio.

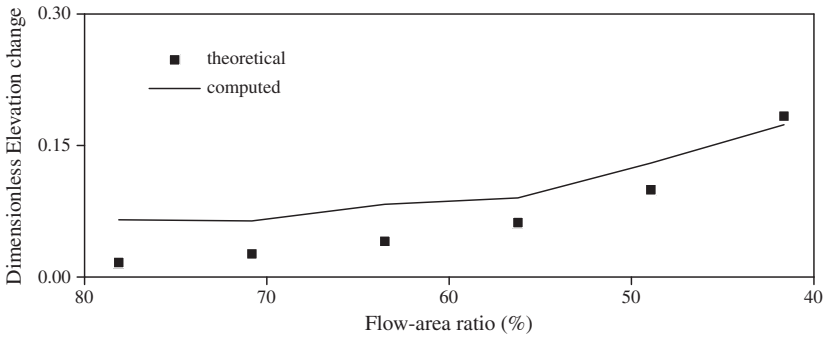


**Fig. 16.** Dimensionless water elevation change with respect to variation of flow-area ratio.

parallel as cases for model evaluation. The flow-area ratio varied with cases is calculated by the ratio of the least cross-sectional area of flow between piers to the cross-sectional area without piers.

To obtain theoretical discharge for comparison, the channel is ideally simplified to a rectangular cross section, and only the continuity equation is considered. Fig. 15 shows the variation of discharge per unit width with respect to the flow-area ratio for both theoretical, which is simply solved by continuity concept (Henderson [27]), and simulation results. Fig. 15 shows that as flow-area ratio equal to 50%, the discrepancy between simulated and theoretical discharge per unit width is about 9.35%. The mass loss is intuitively unavoidable owing that the pier boundary is treated as a source term not a solid boundary. The mass loss increases as the flow-area ratio decreases, therefore, the discrepancy increases between the simulated and theoretical discharge.

Other than the discharge per unit width, the water surface change between the upstream and downstream of the pier is also investigated. The specific energy concept (Henderson [27]) is used to calculate the theoretical water surface change with the assumption of frictionless bed. Fig. 16 shows the theoretical and simulated results of dimensionless water surface change, which is the water surface elevation at upstream minus that at downstream divided by that without pier effect, varied with the flow-area ratio. The discrepancy between simulated and theoretical results is not significant as the flow-area ratio decreases, whereas the largest discrepancy occurred for the largest flow-area ratio. This may be because the specific energy equation with the frictionless bed assumption cannot reveal the phenomenon that water surface is elevated by the flow plunging to the pier. As flow-area ratio decreases, the simulation results approximate to the theoretical ones; it may revealed that the IB method can approximate the theoretical result in less flow-area ratio in spite of the mass loss. This application study indicates that the IB method cannot avoid the mass loss, even with the 4-point $\delta_h$ function**,** but apparently the IB method is proved as an applicable and acceptable technique embedded in a 2-D shallow-water flow model to simulate the water surface change around piers.

## 7. Conclusions

In this study, the proposed model which integrates the IB method with a 2D depth-averaged shallow-water model was conducted to simulate the non-submerged obstacles in open channel flow.

The model's stability is affected by the ratio of marker's mesh width to grid size, which should be greater than 0.6 and 0.7 for the 2-point and 4-point $\delta_h$ functions, respectively. The simulation with the 4-point $\delta_h$ function showed less sensitive to the non-uniformity of marker's distribution than that with the 2-point $\delta_h$ function.

For the cases with uniform grids, the better simulation results can be obtained as the grids are finer in comparison with the experimental data. On the other hand, under the condition of non-uniform grid the simulation error decreases as grid aspect ratio close to 1.0.

As far as the mass conservation concerned, in terms of the mass penetrating through the immersed body, the 4-point $\delta_h$ function gives less mass loss and perform the expected flow pattern behind the body.

The model with the 4-point $\delta_h$ function was verified by a spur dike experiment case. The deflected flow pattern around the spur dike matched well with the experimental data, except the region near the head of the spur dike.

The model capability was examined by the hypothetical cases with multiple parallel piers. The results showed that the mass loss due to the flow penetrating is inevitable, whereas the effect of penetrating quantity is rather small, and the simulation of water surface change gives well agreement with the theoretical results.

Through the studies by capability demonstration and comparison to the experimental data, the application of the IB method in 2-D shallow-water flow computation has been properly validated.

## Acknowledgements

The financial support from the National Science Council (Grant No. NSC 97-2221-E-009-083-MY3) and Water Resources Agency (Grant No. WRA-0980058) is gratefully acknowledged. We also thank the National Center for High-performance Computing, Taiwan, for computer time and facilities.

## Reference

[1] Taylor C, Hughes TG. Finite element programming of the Navier–Stokes equations. Pineridge Press; 1981.
[2] Molinas A, Hafez YI. Finite element surface model for flow around vertical wall abutments. J Fluid Struct 2000;14:711–33.
[3] Mingham CG, Causon DM. Calculation of unsteady bore diffraction using a high resolution finite volume method. J Hydraul Res 2000;38:49–56.
[4] Biglari B, Sturm TW. Numerical modeling of flow around bridge abutments in compound channel. J Hydraul Eng – ASCE 1998;124:156–64.
[5] Tingsanchali T, Maheswaran S. 2-D depth-averaged flow computation near groyne. J Hydraul Eng – ASCE 1990;116:71–86.
[6] Peskin CS. Flow patterns around heart valves: a numerical method. J Comput Phys 1972;10:252–71.
[7] Lai MC, Peskin CS. An immersed boundary method with formal second-order accuracy and reduced numerical viscosity. J Comput Phys 2000;160:705–19.
[8] Silva ALFLE, Silveira-Neto A, Damasceno JJR. Numerical simulation of two-dimensional flows over a circular cylinder using the immersed boundary method. J Comput Phys 2003;189:351–70.
[9] Su SW, Lai MC, Lin CA. An immersed boundary technique for simulating complex flows with rigid boundary. Comput Fluids 2007;36:313–24.
[10] Fadlun EA, Verzicco R, Orlandi P, Mohd-Yusof J. Combined immersed-boundary finite-difference methods for three-dimensional complex flow simulations. J Comput Phys 2000;161:35–60.
[11] Kim J, Kim D, Choi H. An immersed-boundary finite-volume method for simulations of flow in complex geometries. J Comput Phys 2001;171:132–50.
[12] Shen LW, Chan ES. Numerical simulation of fluid-structure interaction using a combined volume of fluid and immersed boundary method. Ocean Eng 2008;35:939–52.
[13] Ahmed F, Rajaratnam N. Flow around bridge piers. J Hydraul Eng – ASCE 1998;124:288–300.
[14] Rajaratnam N, Nwachukwu BA. Flow near groin-like structures. J Hydraul Eng – ASCE 1983;109:463–80.
[15] Warsi ZUA. Fluid dynamics: theoretical and computational approaches. CRC Press; 1999.
[16] Hsieh TY, Yang JC. Investigation on the suitability of two-dimensional depth-averaged models for bend-flow simulation. J Hydraul Eng – ASCE 2003;129:597–612.
[17] Miller S, Chaudhry MH. Dam-break flows in curved channel. J Hydraul Eng – ASCE 1989;115:1465–78.
[18] Lin MY, Huang LH. Velocity profiles of nonlinear shallow-water flows. J Chin Inst Eng 2008;31:105–20.
[19] Falconer RA. Numerical modeling of tidal circulation in harbors. J Waterway Port Coast Ocean Div 1980;106:31–48.
[20] Rastogi AK, Rodi W. Prediction of heat and mass transfer in open channels. J Hydraul Div 1978;104:397–420.
[21] Lien HC, Hsieh TY, Yang JC. Use of two-step split-operator approach for 2D shallow water flow computation. Int J Numer Meth Fluids 1999;30:557–75.
[22] De Vriend HJ. A mathematical model of steady flow in curved shallow channel. J Hydraul Div 1977;15:37–54.
[23] Nezu I, Nakagawa H. Turbulence in open-channel flows. IAHR Monograph Series; 2000. p. 15.
[24] Mittal R, Iaccarino G. Immersed boundary methods. Annu Rev Fluid Mech 2005;37:239–61.
[25] Peskin CS. The immersed boundary method. Acta Numer 2002;11:1–39.
[26] Shin SJ, Huang WX, Sung HJ. Assessment of regularized delta functions and feedback forcing schemes for an immersed boundary method. Int J Numer Meth Fluid 2008;58:263–86.
[27] Henderson FM. Open channel flow. Macmillan; 1966.